Stratocumulus Cloud Clearings and Notable Thermodynamic and Aerosol Contrasts across the Clear–Cloudy Interface

EWAN CROSBIE,* ZHEN WANG,+ ARMIN SOROOSHIAN,*,+ PATRICK Y. CHUANG,# JILL S. CRAVEN,@ MATTHEW M. COGGON,@ MICHAEL BRUNKE,* XUBIN ZENG,* HAFLIDI JONSSON,& ROY K. WOODS,& RICHARD C. FLAGAN,@ AND JOHN H. SEINFELD@

* *Department of Atmospheric Sciences, The University of Arizona, Tucson, Arizona*
+ *Department of Chemical and Environmental Engineering, The University of Arizona, Tucson, Arizona*
# *Earth and Planetary Sciences, University of California, Santa Cruz, Santa Cruz, California*
@ *Department of Chemical Engineering, California Institute of Technology, Pasadena, California*
& *Center for Interdisciplinary Remotely Piloted Aircraft Studies, Naval Postgraduate School, Monterey, California*

(Manuscript received 18 May 2015, in final form 26 November 2015)

ABSTRACT

Data from three research flights, conducted over water near the California coast, are used to investigate the boundary between stratocumulus cloud decks and clearings of different sizes. Large clearings exhibit a diurnal cycle with growth during the day and contraction overnight and a multiday life cycle that can include oscillations between growth and decay, whereas a small coastal clearing was observed to be locally confined with a subdiurnal lifetime. Subcloud aerosol characteristics are similar on both sides of the clear–cloudy boundary in the three cases, while meteorological properties exhibit subtle, yet important, gradients, implying that dynamics, and not microphysics, is the primary driver for the clearing characteristics. Transects, made at multiple levels across the cloud boundary during one flight, highlight the importance of microscale (~1 km) structure in thermodynamic properties near the cloud edge, suggesting that dynamic forcing at length scales comparable to the convective eddy scale may be influential to the larger-scale characteristics of the clearing. These results have implications for modeling and observational studies of marine boundary layer clouds, especially in relation to aerosol–cloud interactions and scales of variability responsible for the evolution of stratocumulus clearings.

1. Introduction

Large clearings (>100 km in width) in the stratocumulus cloud deck capping the marine boundary layer are often found off the western coast of the United States (e.g., Kloesel 1992). The frequency, temporal persistence, and nature of how these clearings develop and evolve are unclear. The presence of clearings in an otherwise cloudy marine boundary layer motivates the question concerning the extent to which similarity exists between environmental properties on each side of the clear–cloudy boundary. Identifying the governing factors and their relative importance in explaining the clearings has implications for general studies of aerosol–cloud–precipitation–radiation interactions and modeling of marine boundary layer clouds, in addition to being helpful for operational forecasting of weather and fog along coastlines.

The organizational morphology of marine stratocumulus clouds is regulated by a complex interplay between radiation, dynamics, cloud and aerosol microphysics, and surface fluxes (Wood 2012). Internal feedbacks can have a buffering effect to stabilize the cloud system against changes in the large-scale environment (e.g., Zhu et al. 2005), illustrative in the spatial extent and homogeneity of marine cloud decks. However, patterns in large-scale dynamic forcing (i.e., lower-tropospheric subsidence and divergence, midlatitude disturbances), surface properties (i.e., sea surface temperature), and aerosol concentration/properties can induce marked transitions in the mesoscale organization of the cloud field (Albrecht et al. 1995; Bretherton and Wyant 1997; Stevens et al. 2005; Wang and Feingold 2009) or the thinning or ultimate dissipation of the cloud

Corresponding author address: Armin Sorooshian, The University of Arizona, P.O. Box 210011, Tucson, AZ 85721.
E-mail: armin@email.arizona.edu

DOI: 10.1175/JAS-D-15-0137.1

layer by enhanced subsidence (Randall and Suarez 1984; Zhang et al. 2009), which can be forced on the mesoscale by coastal topographic interactions (Sunuararajan and Tjernström 2000; Brooks et al. 2003).

Clearing events, such as the examples shown in Fig. 1, allow airborne research flights to characterize vertically resolved differences on both sides of the clear–cloudy interface to help facilitate an understanding of the multiscale dynamic and microphysical processes that control their extent and longevity. Such an understanding can be used to improve parameterization of boundary layer clouds in global models, as accurate prediction of regional patterns in low-cloud-fraction scenes is a critical component in reducing uncertainties related to cloud effects on climate (Bony and Dufresne 2005; Bony et al. 2006; Wyant et al. 2006; Soden and Vecchi 2011), specifically in quantifying departures from typical climatological patterns of stratocumulus (e.g., Klein and Hartmann 1993). Vertically resolved observations at the clear–cloudy boundary can test assumptions used in studies of aerosol–cloud interactions with remote sensing data. Traditionally, remotely sensed parameters relevant to aerosol particles are derived from cloud-free scenes (e.g., Martins et al. 2002; Remer et al. 2012); this becomes problematic for aerosol–cloud interaction studies that rely on the assumption that aerosol properties in clear-air scenes are representative of those in the cloudy column that are most likely influenced predominantly by subcloud particles rather than those above cloud. However, this assumption can be affected by a number of factors such as spatial heterogeneity in the boundary layer, aerosol layers above cloud, and processes such as wet scavenging below cloud that can preferentially impact either the cloudy or clear column (Duong et al. 2011). As shown in other studies, aerosol physicochemical properties and relative humidity (RH) can change when transitioning from cloud-free areas to cloudy areas (Twohy et al. 2009; Wang and Geerts 2010; Bar-Or et al. 2012; Wonaschütz et al. 2012; Altaratz et al. 2013) or remain relatively unchanged (e.g., Stevens et al. 2005; Sharon et al. 2006), which can impact both the calculated magnitude of radiative effects of aerosol and retrievals of aerosol and cloud parameters (Chand et al. 2012).

In this work we study three case flights across clearings of varying dimensions off the California coast. We aim to address the following: (i) the formation, evolution, and frequency of the clearings; (ii) the extent to which reanalysis data can capture long-lived clearings as compared to remote sensing data; (iii) vertical and horizontal variability in dynamic, thermodynamic, and aerosol properties on both sides of a clear–cloudy boundary; and (iv) possible mechanisms responsible

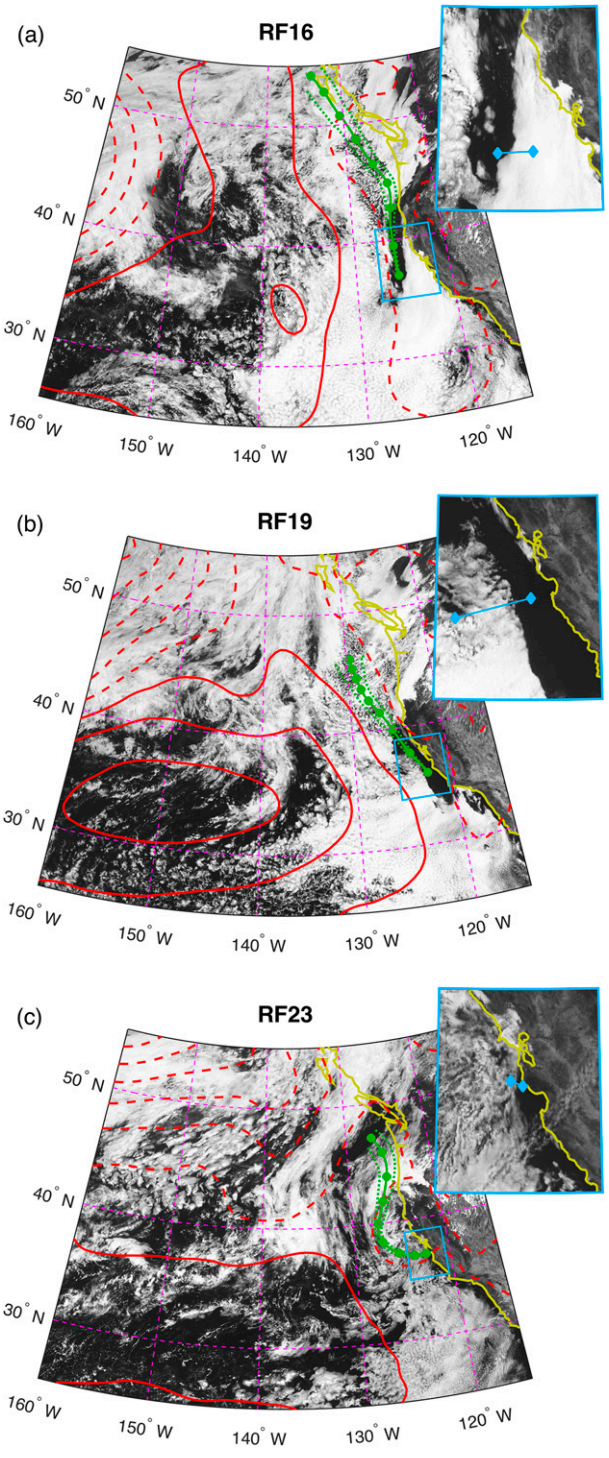

FIG. 1. *GOES-15* visible-band imagery at times relevant to each case flight: (a) RF16: 1900 UTC 29 Jul, (b) RF19: 1900 UTC 1 Aug, and (c) RF23: 2300 UTC 7 Aug. The following are overlaid on each panel: (i) 850-hPa geopotential height contours from MERRA (red; 3-dm increments with dashed contours showing heights below 156 dm); (ii) ensemble-mean 72-h back trajectories (solid green) at 6-hourly increments (green marker) ending at 500 m, with $\pm 1\sigma$ ensemble lateral variability measured normal to the mean trajectory path (dashed green); (iii) inset is an expanded view of the clearing with approximate location of the clear–cloudy transect (blue).

for the variability in the spatial arrangement of clearings.

2. Experimental data

a. Instrument payload

The Nucleation in California Experiment (NiCE) consisted of 23 flights with the Center for Interdisciplinary Remotely Piloted Aircraft Studies (CIRPAS) Twin Otter based out of Marina, California, during July and August 2013. The purpose of the field campaign was to investigate both aerosol–cloud–precipitation–radiation interactions and nucleation in both marine and continental atmospheric conditions.

The aircraft payload is described in another NiCE study (Coggon et al. 2014) including (i) meteorological data [e.g., temperature, humidity, winds, Gerber probe liquid water content (LWC; Gerber et al. 1994)], (ii) cloud and aerosol spectrometer (particle diameter $D_p \sim$ 1–55 μm; Droplet Measurement Technologies, Inc.; Baumgardner et al. 2001) and cloud imaging probe (CIP; $D_p \sim$ 25–1550 μm) for drop size distributions, (iii) condensation particle counter (CPC 3010; TSI Inc.; $D_p \geq 10$ nm) and a passive cavity aerosol spectrometer probe (PCASP; PMS Inc./DMT Inc.; $D_p \sim$ 0.1–2.6 μm) for particle number concentrations, (iv) Aerodyne compact time-of-flight aerosol mass spectrometer (C-ToF-AMS; Drewnick et al. 2005) for submicrometer mass concentrations of nonrefractory aerosol constituents, (v) cloud water collection with a modified Mohnen slotted-rod cloud water collector (Hegg and Hobbs 1986) followed by ion chromatography and inductively coupled plasma mass spectrometry analysis (Sorooshian et al. 2013), (vi) cloud condensation nuclei counter (CCNc; Droplet Measurement Technologies; Roberts and Nenes 2005), and (vii) scanning mobility particle sizer (SMPS) comprising a differential mobility analyzer (DMA Model 3081, TSI Inc.) coupled to a CPC (Model 3010, TSI Inc.). The time resolution is 1 Hz or faster for the measurements described above with the exception of the SMPS (73-s response time) and C-ToF-AMS (~10 s). The effective CCN activation diameter D_{act} is computed by integrating the SMPS number size distributions from the largest size down to the size at which the concentration is equivalent to that of the CCNc at 0.2% supersaturation. Lower D_{act} values (at fixed supersaturation) are indicative of more favorable composition for drop activation at smaller dry-particle sizes.

Fast winds were measured using a five-hole gust probe radome connected to Setra pressure transducers, which were then coupled to measurements of platform motion using a C-MIGITS-III GPS/INS system. Total temperature was measured using a Rosemount model 102 total temperature sensor, from which static air temperature was calculated. Humidity was measured using an EdgeTech Vigilant chilled mirror hygrometer. The three wind components and temperature had time responses faster than 10 Hz and the analog outputs were time averaged to 10 Hz to synchronize with the INS, while the humidity was slower (1–2 s). No correction was made to temperature measurements to account for cloud water, but measured humidity measurements in excess of 100% RH were capped at saturation.

Aerosol data are reported only when LWC $< 0.02\ \mathrm{g\ m^{-3}}$ (in-cloud threshold) in order to avoid biases owing to droplet shattering (Shingler et al. 2012). Cloud albedo is estimated using cloud optical depth τ: $A = \tau/(\tau + 7.7)$ (Lacis and Hansen 1974), which is derived from the cloud droplet distribution [Chen et al. (2012) and references therein] and represents an estimate of cloud albedo at cloud top. The free-tropospheric dewpoint depression is computed as the average difference between ambient temperature and dewpoint temperature over the region from 100 m above the cloud top to the highest point reached in soundings (Chen et al. 2012). Cloud-base rain rate is derived from CIP measurements above cloud base. Inversion-base height is defined as the altitude where temperature first reaches a minimum above the surface and the top is defined as the height that the 5-s running mean of $d\theta/dz$ reaches a maximum. Inversion strength is the difference of potential temperature between the inversion-top and -base heights.

b. Flight sampling strategy

This study focuses on three specific research flights (RFs): RF16 on 29 July 2013, RF19 on 1 August 2013, and RF23 on 7 August 2013. Two of these flights (RF16, RF19) consisted of a single leg from Marina to the west followed by sampling maneuvers on the two sides of a clear–cloudy boundary (known as the "clear–cloudy module"), which ended with a reverse leg back to Marina. The third flight consisted of two subflights in rapid succession with fueling in between, with one carried out flying north in the California Central Valley and landing at Arcata near the California–Oregon border. The second subflight on this day consisted of flying south over the Pacific Ocean toward Marina with a clear–cloudy module close to the end of the flight and located near the coast. Clear–cloudy modules occurred midday for RF16 (1845–2000 UTC) and RF19 (1745–1915 UTC) and later in the afternoon for RF23 (2245–2345 UTC). Regional patterns in the cloud cover are visualized using *GOES-15* visible-band imagery, at times concurrent with the aircraft observations (Fig. 1).

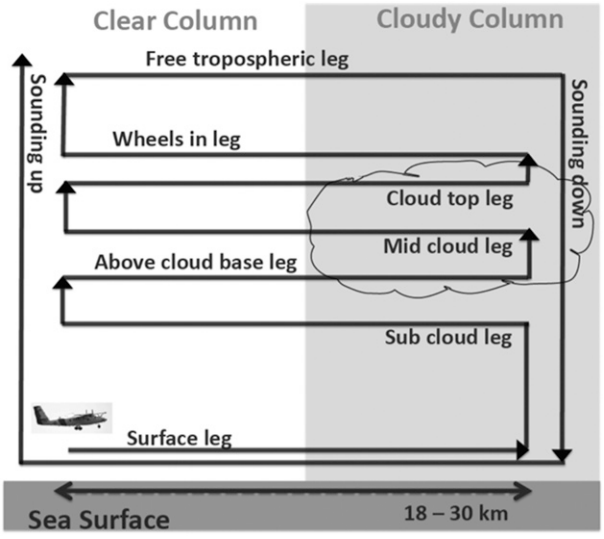

FIG. 2. Schematic of the Twin Otter flight strategy for the cloudy–clear module with level legs and soundings conducted on both sides of a distinct stratocumulus cloud boundary. The order of the module components was reversible and altitudes were selected to suit the individual case.

In each case, the aircraft flight plan for the clear–cloudy module (Fig. 2) consisted of (i) vertical soundings in the clear and cloudy columns and (ii) level legs below, in, and above clouds that extended beyond the cloud edge and into the clear side. Two legs were usually conducted above cloud top, including one immediately above the top called the ''wheels in'' leg, and another approximately 150 m above cloud top that will be referred to as the ''free tropospheric (FT)'' leg. The duration of the legs was approximately 5 min (~15 km) on each side of the clear–cloudy boundary.

3. Results and discussion

a. Clearing description

At their widest points, the clearings sampled during RF16, RF19, and RF23 were approximately 150, 300, and 30 km, respectively (Fig. 1). The clearing observed during RF16 was mostly detached from the coast with predominantly closed-cell stratocumulus and coastal stratus to the east, whereas clearings observed during RF19 and RF23 extended offshore from the California coastline. *GOES-15* visible imagery during the period before and through RF16 and RF19 reveal key details about the nature of the progression of the clearings moving south along the majority of the length of the western United States, aligned with the long axis nearly parallel to the mean wind direction. GOES imagery was used to estimate the total area and centroid of the clearings at 0000 UTC (afternoon) and 1500 UTC (morning) each day from 24 July to 3 August (Fig. 3) and revealed that the clearings probed during RF16 and RF19 were associated with a single long-lived clearing event. RF23 sampled a local coastal clearing with no evidence of a contiguous multiday presence.

Analysis of the satellite data during the 96 h preceding RF16 suggests the continuous presence of a clear-air region, which migrated slowly southward from an initial position near the coast of British Columbia, Canada. The clearing exhibited two modes illustrated in Fig. 3: the first relating to the slow southward migration and the second relating to the diurnal expansion (day) and contraction (night) of the clearing, which was aligned with the commonly observed thinning (day) and thickening (night) cycle of marine stratocumulus (e.g., Wood et al. 2002). The clearing centroid moved closer to the coastline during the night. The relatively slow (approximately $3\,m\,s^{-1}$) southward migration of the clearing compared with the mean flow ($8–15\,m\,s^{-1}$ based on mean trajectory motion) is suggestive of a dynamic forcing and/or a mixing mechanism, rather than simply advection of a different air mass. In the 24 h following RF16, the clearing filled in almost completely before a clearing reformed during the day prior to RF19. Therefore, RF16 occurred during a decay phase in the 11-day life cycle of the clearing and RF19 marked a growth phase.

It is possible that the clearings observed during RF16 and RF19 can be traced to the same forcing mechanism; however, the reason for the hiatus on 30 July remains unclear. During RF19 the clearing was attached to the coastline and was flanked to the west by closed-cell stratocumulus with embedded pockets of open cells, which then transitioned to a predominantly open-cell regime farther west. RF23 conversely included a much smaller clearing closer to the coast with drizzle in the study region and a decoupled layer below cloud base and likely resulted in a thinning cloud layer prior to sampling. GOES imagery for RF23 confirms that there is a less-distinct clear-air region that likely stemmed from more localized effects. The distinct difference in the size and evolution of the three cases suggests that there may be multiple driving mechanisms responsible for clearings that operate at difference scales.

Reanalysis data from NASA's Modern-Era Retrospective Analysis for Research and Applications (MERRA; Rienecker et al. 2011) offer insight into the large-scale circulation patterns, which may influence the formation and location of clearings. The low-level synoptic-scale circulation pattern is assessed using the 850-hPa geopotential heights overlaid on the satellite imagery (Fig. 1). During RF16, the subtropical ridge

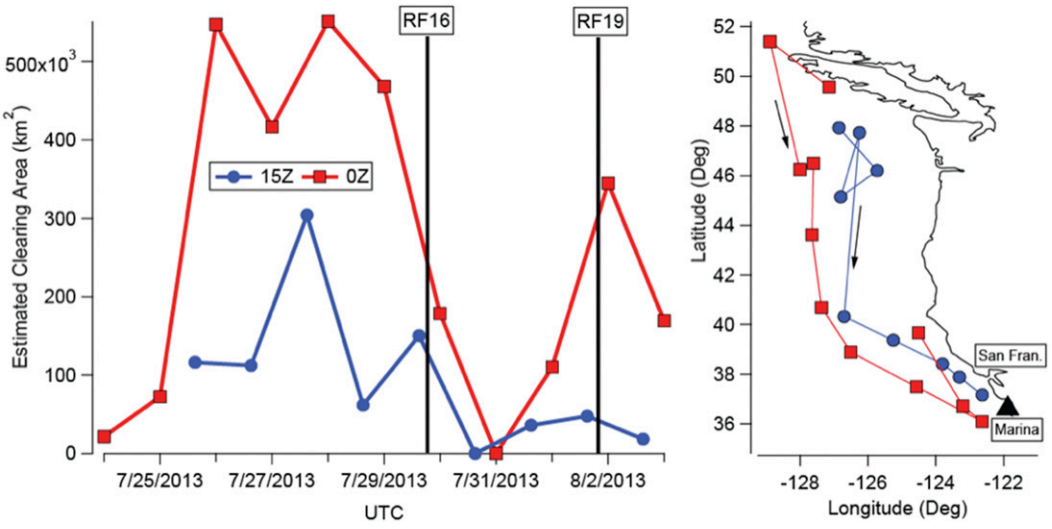

FIG. 3. (left) Estimated clearing area at 0000 UTC (afternoon) and 1500 UTC (morning) for a 10-day period including RF16 and RF19. (right) Movement of the clearing centroid from 24 Jul through 3 Aug with each marker corresponding to one in the left panel with movement generally down parallel to the coast with time and toward the coast at night and early morning.

extends along the coast of western North America elongated along a north–south axis with an approaching closed low pressure system to the west. By RF19, the flow around the ridge is more zonal and its position has shifted to the south and strengthened. By RF23, the ridge is farther south and weaker. The exact pattern associated with the subtropical ridge may influence the formation and persistence of clearings through locally increased subsidence associated with anticyclonic curvature, mesoscale interactions with the coastal topography, and diurnal sea-breeze circulations. Headlands along the California coast have been shown to strongly affect the low-level circulation and boundary layer characteristics (e.g., Koracin and Dorman 2001; Brooks et al. 2003) and may act as focal points for preferred clearing arrangements. Once a clearing is established, the horizontal discontinuity in the longwave flux at the cloud boundary may then induce an organized convective circulation pattern near the edge. Horizontal entrainment of clear air may support a positive feedback mechanism, associated with buoyancy reversal depending on the thermodynamic properties of the clear air, leading to rapid changes in the extent of the clearing on diurnal time scales. This will be explored in more detail in the discussion of RF16 and RF19.

Out of 23 flight days during NiCE, seven flights were characterized as having clearings similar to those in RF16 and RF19, which are defined in this study as having a minimum clearing width and length of 150 and 300 km, respectively, at their maximum values in that same spatial area at 1915 UTC; to identify a clearing, it was of course necessary for there to be clouds and another criteria was that cloud fraction (CF) over water had to exceed 30% in an area defined by 35°–40°N and 120°–130°W (MODIS *Aqua* and *Terra*; level-3 daily product). In a previous study in the same region and same months of a different year [Eastern Pacific Emitted Aerosol Cloud Experiment (E-PEACE) 2011; Russell et al. 2013]. these events were observed in 15 out of 30 flight days. Thus, such events can be considered frequent for this region during the summertime.

b. *Comparison of MODIS and MERRA*

Since the clearings in RF16 and RF19 are frequent, spatially large, and temporally persistent, it is of interest to determine the extent to which they are captured by global reanalysis data. Spatial distributions of cloud fraction and LWP over the eastern Pacific Ocean (35°–45°N, 122°–130°W) from MERRA do not match the location of the clearings that are evident from the GOES imagery and MODIS *Terra* data (Fig. 4). However, MERRA does show evidence of reduced cloud fraction and LWP in other parts of the spatial domain examined. To address the impact on large-scale radiative forcing, a comparison is made between the regional mean cloud fraction and LWP from MERRA versus MODIS *Terra* for the region shown in Fig. 4. Table 1 reports that the spatially averaged cloud fraction is nearly identical between MODIS and MERRA for RF19 and RF23 and is about 10% less for MERRA in RF16. LWP is also nearly identical between MODIS and MERRA for RF19 and RF23, but the MERRA value only equates to

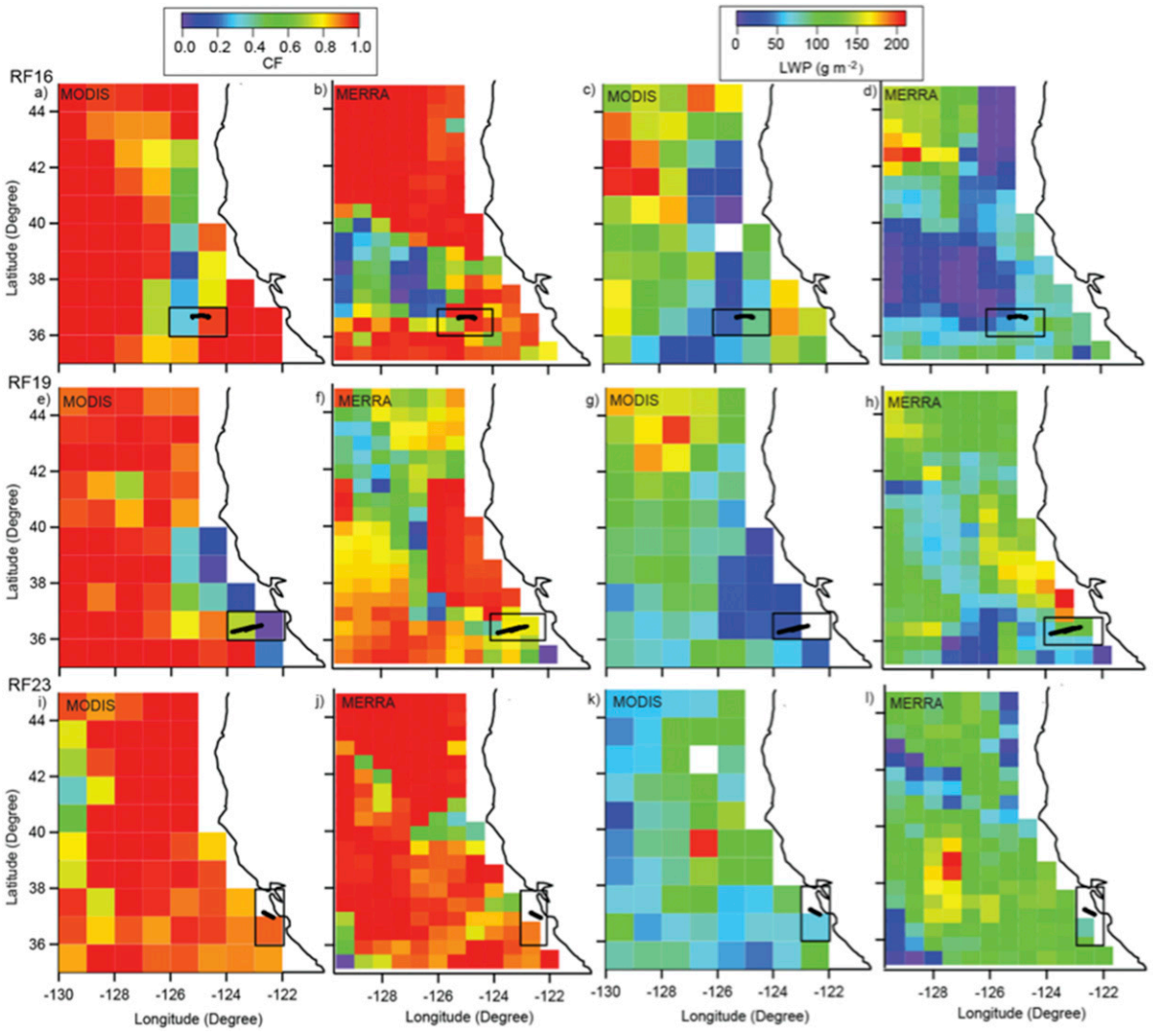

FIG. 4. Comparison of MODIS *Terra* (level-3 daily product) and MERRA CF and cloud liquid water path (LWP) for each case flight. The MERRA cloud fractions are the hourly mean centered at 1930 UTC (close to *Terra* overpass time), while the LWPs are instantaneous values at 1900 UTC. The black line placed in the boxes in each panel refers to the flight tracks across the clear–cloudy border. The bulk average of cloud fraction and LWP for the full study region using MODIS and MERRA are shown in Table 1.

about 39% of the MODIS value for RF16. The discrepancy in the spatial identification of the clearing and, at times, values of cloud fraction and LWP motivates a deeper investigation of environmental properties near the clearings. It is likely that the clearings are partially driven by subgrid processes (e.g., cloud microphysics and boundary layer dynamics), which can upscale to more climatologically influential sizes.

c. *Aerosol and airmass sources*

Two-day backward trajectories computed using the NOAA HYSPLIT model (Draxler and Hess 1997) (Fig. 1) support marine airmass origins in all three flights and were consistent with aircraft-measured winds. Trajectories were computed at an end altitude of 500 m MSL to simulate an approximate level relevant to the cloud layer for 54 ensemble members, which included meteorological grid perturbations (see HYSPLIT user guide for details: http://www.arl.noaa.gov/documents/reports/hysplit_user_guide.pdf) and inclusion of the GDAS and NAM gridded data. Ensemble-mean positions were calculated using all ensemble members at hourly increments and, for each increment, the standard deviation ($\pm 1\sigma$) of the position of ensemble members orthogonal to the mean trajectory path was used as an estimate of the ensemble spread. The trajectory paths are aligned with the MERRA 850-hPa geopotential height patterns, which are also overlaid in Fig. 1. That

TABLE 1. Comparison of CF and LWP between MODIS *Terra* and MERRA for the marine region inside 35°–45°N, 122°–130°W (Fig. 4). Averages and standard deviations (in parentheses) are reported for data obtained at the time of each flight.

	Cloud fraction		LWP ($g\,m^{-2}$)	
Flight	MODIS	MERRA	MODIS	MERRA
RF16	0.88 (0.20)	0.79 (0.29)	116.9 (59.8)	45.6 (34.8)
RF19	0.84 (0.27)	0.85 (0.13)	93.7 (44.3)	91.4 (21.7)
RF23	0.91 (0.12)	0.92 (0.12)	84.1 (28.9)	78.5 (26.9)

said, eddy-overturning circulations associated with land–sea thermal contrasts are likely underrepresented owing to the resolution of the GDAS and NAM data used as an input for HYSPLIT and may contribute to the mixing of continental sources into the predominantly marine trajectories. In addition, the prominent coastal topography of Northern California may induce additional mechanisms for lateral mixing (such as coastal eddies and mountain–valley circulations), which may also influence the trajectories.

Cloud water chemical composition data confirm a strong influence from sea salt for at least the first two flights when the cloud layer was not decoupled from the surface layer: Na^+ and Cl^- collectively accounted for 83% and 66% of the total measured air-equivalent mass concentration in RF16 and RF19, respectively (Fig. 5). RF23 cloud water exhibited the lowest total mass concentration ($3.6\,\mu g\,m^{-3}$ versus 18.0–$71.2\,\mu g\,m^{-3}$ in RF16 and RF19) due, in part, to scavenging of aerosol mass by drizzle and subsequent decoupling of the subcloud layer. Aside from sea salt, contributions from acidic components such as sulfate, nitrate, and organic acids stem from emissions of their precursors from sources such as ships and marine biota (Prabhakar et al. 2014; Wang et al. 2014).

Subcloud CPC number concentrations were below about $400\,cm^{-3}$ on the two sides of the clear–cloudy boundary, indicative of minimal influence from fresh anthropogenic pollution (e.g., ship or continental plumes). However, this does not preclude the influence from aged anthropogenic pollution, especially from ship traffic, which usually impacts marine boundary layer aerosol in this exact study region (Coggon et al. 2012; Wonaschütz et al. 2013). Subcloud PCASP concentrations ranged between 185 and $279\,cm^{-3}$ in the three flights. CPC and PCASP concentrations in the FT leg ranged between 78–1150 and 48–$952\,cm^{-3}$, respectively. Subsequent sections will discuss the significant differences between subcloud and above cloud areas and also horizontal gradients along level legs, as they have implications for use of surface measurements or vertically integrated remote sensing data to study aerosol–cloud interactions.

d. Case study 1: Research flight 16 (29 July 2013)

1) METEOROLOGICAL AND THERMODYNAMIC SPATIAL PROFILES

RF16 is the lone case with clouds on the eastern side of the clear–cloudy interface. Similar patterns have been observed in conjunction with the northward advancement of cool stratified air, termed ''stratus surge'' or ''southerly surge,'' recirculated along coastal California and cooled from below by local sea surface temperature (SST) minima (Mass and Albright 1987; Mass et al. 1986; Felsch and Whitlatch 1993). A reversal in the near-surface meridional wind from northerly to southerly was observed within 100 km of the California coast during RF16 consistent with previous studies of coastally trapped wind reversals (e.g., Mass and Bond 1996; Nuss et al. 2000; Rahn and Parish 2010) and can be attributable at the synoptic scale to a northwestward migration of the thermal trough located over the interior United States (Mass and Bond 1996; Brewer et al. 2012), which is evident in the 850-hPa geopotential height field (Fig. 1). Importantly, the boundary layer wind reversal was not collocated with the cloud boundary; rather, it was displaced 170–200 km to the east, such that the cloud boundary was in a region of northwesterly flow. In the vicinity of the clearing, the cloudy column on this flight was the thickest among the three case studies (base around 440 m, top around 680 m), with the highest LWP ($\sim 75\,g\,m^{-2}$), lowest column-mean drop effective radius ($r_e = 8.9\,\mu m$), highest cloud optical depth (14.9), and highest albedo (0.63) (Table 3). Interestingly, very minor differences were observed below cloud for the following environmental variables on the two sides of the clear–cloudy boundary (Tables 2 and 3): aerosol properties (size distribution, composition, hygroscopicity), wind speed, and SST. Turbulent kinetic energy (TKE) exhibited perhaps the most significant difference in the boundary layer between the two sides of the boundary with higher values on the cloudy side at all altitudes below the wheels-in leg (Table 2), driven presumably by buoyancy production of TKE, caused by cloud-top radiative cooling on the cloudy side.

The vertical profiles of potential temperature and specific humidity are almost the same on the clear and cloudy sides in the subcloud layer (Fig. 6). The clear-air sounding is slightly warmer than the cloudy sounding at the altitudes where the cloud exists, which is then manifested as a (marginally) statically stable profile extending below cloud. A subtle feature exists at altitudes near cloud top as the clear-side potential

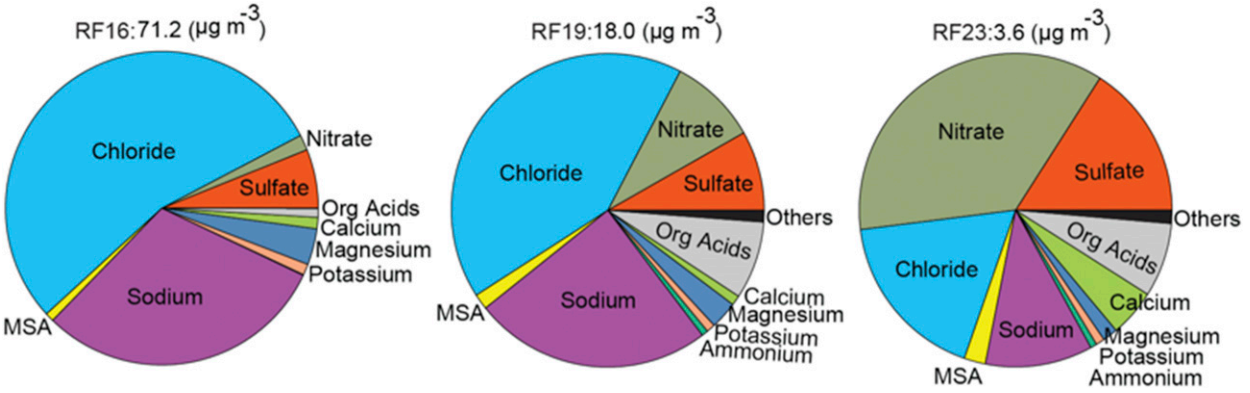

FIG. 5. Comparison of water-soluble cloud water composition (via ion chromatography) in the three case flights. The total mass concentration (sum of water-soluble species) in each case is shown above each pie.

temperature shows warming (2–3 K) and drying (1 g kg^{-1}) in the layer equivalent to the upper 100 m of the cloud. In the absence of cloud, entrainment warming and drying is not balanced by cloud-top radiative cooling and a lack of mixing from below allows this feature to persist. This is further supported by negative buoyancy production and reduced TKE observed on the clear side from subcloud altitudes up to wheels-in leg compared with the cloudy column (Table 2). Since the air in the clear column above the inversion is both cooler and moister, this suggests a further byproduct of entrainment/mixing eroding the cloud, but it firmly rejects increased subsidence/divergence in the clear region as the forcing mechanism, because this would lead to warmer and/or drier conditions above cloud. Moister air above the clearing may also reduce the effectiveness of longwave radiative cooling to reinvigorate boundary layer mixing and reestablish or extend cloud into the clearing. With such a subtle difference between clear and cloudy columns, one may hypothesize that if a cloud layer were reestablished the clear sounding would quickly resort back to the profile seen on the cloudy side. The satellite data confirm that this is indeed what happens (Fig. 3), with the stronger nocturnal radiative forcing being the necessary mechanism to completely fill in the clearing.

2) AEROSOL SPATIAL PROFILES

The major difference on the two sides of the clear–cloudy boundary was the higher particle concentration in the wheels-in leg on the cloudy side versus the clear side (CPC: 647 versus 481 cm^{-3}). PCASP size distributions illustrate this enhancement between 130 and 175 nm (Fig. 7), and the source does not appear to be the FT based on comparing PCASP distributions and concentrations of CCN and sulfate but, instead, likely stems from cloud processing. Previous work in the region has shown the presence of residual layers of cloud-produced species above cloud tops (Sorooshian et al. 2007) and lofted residual layers during boundary layer collapse (Berner et al. 2015). Free-tropospheric size distributions differ from other altitudes because the accumulation mode above a diameter of 100 nm is absent.

The subcloud aerosol composition, CCN concentrations (0.2% SS), and D_{act} values were similar on the clear and cloudy sides (Table 2). Sulfate was the dominant nonrefractory species in the submicrometer aerosol, with similar concentrations up until the free troposphere where it dropped in contrast to organics, which increased. CCN concentrations decreased significantly in the FT (36 cm^{-3} on the cloudy side and 16 cm^{-3} on the clear side) relative to lower-altitude legs simultaneous with an increase in D_{act} (234 nm on the cloudy side and 167 nm on the clear side), suggestive of fewer CCN-active aerosols and thus less-favorable composition (i.e., more organics, less sulfate) for drop activation. Previous work in the region also provided evidence of suppressed subsaturated aerosol hygroscopicity above cloud top due to enhanced organic mass fractions (Hersey et al. 2009).

e. Case study 2: Research flight 19 (1 August 2013)

1) METEOROLOGICAL AND THERMODYNAMIC SPATIAL PROFILES

RF19 resembles RF16 in that near-surface environmental variables were similar on both sides of the clear–cloudy boundary (aerosol properties, wind speed, and SST) with enhanced TKE on the cloudy side (Tables 2 and 3), with the exception of the moisture profile, which was considerably drier on the clear side. Relative to RF16, the cloud deck had a higher base height (~660 m), reduced thickness (170 m) and LWP (~50 g m^{-2}), higher column-mean N_d (~160 cm^{-3}), higher column-mean r_e (9.2 μm), lower optical thickness (10.2), and similar

TABLE 2. Level leg-average values of environmental parameters. Numbers before/after slashes represent the average for the clear/cloudy part of each leg. A long dash in cloud indicates data omitted owing to the potential influence of drop shatter effects on their measurement. Blank cells indicate that a level leg was not conducted at that altitude in a particular flight. BP = buoyancy production; all other abbreviations defined in the text.

	Subcloud	Above cloud base	Midcloud	Wheels in	FT
RF16					
Altitude (m)	525	586	599	695	765
TKE $\times 10^3$ ($m^{-2}s^{-2}$)	15/338	32/362	6/193	17/80	1/21
BP $\times 10^6$ ($m^{-2}s^{-3}$)	−49/135	−30/227	−41/329	−68/−26	−20/−66
PCASP (cm^{-3})	198/191	181/—	206/—	219/239	131/87
CPC (cm^{-3})	379/378	379/—	386/—	481/647	608/636
$CCN_{SS=0.2\%}$ (cm^{-3})	161/160	149/—	160/—	156/117	36/16
D_{act} (nm)	81/84	160/—	99/—	74/84	167/234
AMS Org ($\mu g\,m^{-3}$)	0.6/0.7	0.7/0.4	0.7/0.5	0.7/0.8	0.9/NA
AMS SO_4 ($\mu g\,m^{-3}$)	1.2/1.3	1.2/0.5	1.2/0.5	1.1/0.9	0.2/0.2
RF19					
Altitude (m)	586	661	706	805	949
TKE $\times 10^3$ ($m^{-2}s^{-2}$)	56/394	83/504	35/400	57/357	22/22
BP $\times 10^6$ ($m^{-2}s^{-3}$)	−30/250	−27/339	−11/293	−27/−314	−44/−24
PCASP (cm^{-3})	185/192	180/—	179/—	174/639	417/952
CPC (cm^{-3})	210/247	202/—	163/—	192/696	667/1150
$CCN_{SS=0.2\%}$ (cm^{-3})	101/127	100/—	71/—	95/237	165/387
D_{act} (nm)	140/160	140/—	134/—	117/122	184/128
AMS Org ($\mu g\,m^{-3}$)	0.5/0.5	0.4/—	0.5/0.9	0.8/3.5	2.9/4.4
AMS SO_4 ($\mu g\,m^{-3}$)	0.4/0.4	0.4/0.2	0.3/0.4	0.4/0.9	0.5/1.1
RF23					
Altitude (m)	278		431	553	718
TKE $\times 10^3$ ($m^{-2}s^{-2}$)	233/336		130/339	86/37	226/38
BP $\times 10^6$ ($m^{-2}s^{-3}$)	−40/25		−232/−33	99/57	−123/−22
PCASP (cm^{-3})	279/214		24/—	13/8	130/48
CPC (cm^{-3})	283/246		147/—	92/54	439/78
$CCN_{SS=0.2\%}$ (cm^{-3})	57/54		13/—	5/7	17/8
D_{act} (nm)	55/97		100/—	265/294	179/228
AMS SO_4 ($\mu g\,m^{-3}$)	0.5/0.5		0.1/0.2	0.1/0.1	0.2/0.4

cloud base rain rate (0.1 mm day^{-1}) and albedo (0.59) (Table 3).

Vertical profiles on RF19 differ from RF16 in the following ways: (i) erosion in the temperature inversion occurred lower in the clear column relative to where cloud top was in the cloudy column, (ii) the moisture profile in the clear sounding was drier than the cloudy side, and (iii) above the inversion, clear air is both warmer and drier than the cloudy column, suggesting that the extent of previous boundary layer mixing was confined at or below the current cloud top, potentially as a result of increased localized subsidence/divergence in the clear region. The inversion base and top heights were considerably lower on the clear side (versus the cloudy side) with a weaker estimated inversion strength (2.3 K on clear side versus 3.6 K on cloudy side). The data suggest that there may have been entrainment of dry air from aloft on the clear side, which is supported by a high dewpoint-depression value (23.3 K) and negative buoyancy production values along the entire vertical clear column. The coastal arrangement of the clearing during RF19 (Fig. 1), compared with RF16, is also likely to promote more interaction with dry continental air.

The comparison between the clear and cloudy soundings in RF19 provides insight into the rapid expansion of the clearing around the time it was sampled (Fig. 3). As alluded to in section 3a, theoretical arguments for conditional instability, as a result of mixing between cloudy and clear air (e.g., Randall 1980; Deardorff 1980) can justify the formation of evaporatively cooled downdrafts. Although this mechanism, referred to as cloud-top entrainment instability (CTEI), has been shown to have limited explanatory power for widespread cloud break up when considered in isolation of other, perhaps more dominant, mechanisms (Mellado et al. 2009; Mellado 2010; Carman et al. 2012; Gerber et al. 2013), it does provide a framework for expressing the susceptibility of producing negatively buoyant mixtures. A nondimensional instability parameter κ is defined as follows (Kuo and Schubert 1988):

TABLE 3. Summary of average environmental properties based on sounding data in adjacent clear and cloudy columns for three case flights.

		Cloudy			Clear		
		RF16	RF19	RF23	RF16	RF19	RF23
Above cloud	Dewpoint depression (K)	25.9	23.3	0.19			
	Inversion-base height (m)	680	820	580	600	700	330
	Inversion-top height (m)	690	840	720	690	750	350
	Inversion strength (K)	2.8	3.4	2.4	3.6	2.8	0.6
Cloud	Depth (m)	240	170	150			
	Column-mean N_d (cm^{-3})	136	158	54			
	Column-mean r_e (μm)	8.9	9.2	14.3			
	Optical depth	14.9	10.2	7.6			
	LWP ($g\,m^{-2}$)	74	52	61			
	Base rain rate ($mm\,day^{-1}$)	0.1	0.12	1.2			
	Albedo	0.63	0.59	0.48			
Near surface	SST (°C)	14.9	15.4	14.6	14.8	15.4	14.6
	Wind ($m\,s^{-1}$)	9.6	7.4	4.5	9.3	7.4	4.5

$$\kappa = \frac{c_p \Delta\theta_e}{L_v \Delta q_t}, \tag{1}$$

where c_p is the specific heat capacity of water at constant pressure, L_v is the enthalpy of vaporization of water, and $\Delta\theta_e$ and Δq_t are the jumps in θ_e and total water mixing ratio, respectively. We calculate κ for each of the respective vertical and horizontal jumps at the cloud edge (Table 4), with higher values more likely to yield unstable cloudy–clear mixtures. We use the stringent approximation of an adiabatic cloud layer to estimate q_t in the cloud using the mean subcloud vapor mixing ratio. The comparison between the κ conditions is suggestive that the horizontal entrainment of dry air at cloud edge may play an important role in producing evaporatively cooled downdrafts, which accelerates the erosion of the cloud edge (Fig. 3). In RF16, the jump in equivalent potential temperature θ_e is positive away from the cloud both vertically and horizontally, suggesting stability of the cloud edge, whereas in RF19 it is negative (Table 4).

2) AEROSOL SPATIAL PROFILES

Particle number concentrations were uniform in the clear column (e.g., PCASP between 174 and 185 cm^{-3}) up until the FT leg when concentrations increased by more than a factor of 2 to 417 cm^{-3} (Table 2). But the most striking aerosol feature was the remarkable enhancement (more than factor of 3) in number concentration in the cloudy column above the cloud. The PCASP size distributions illustrate the sharp enhancement between 140 and 175 nm in the wheels-in and FT legs; unlike RF16, there is sharp similarity between these two altitudes suggestive of transported continental pollution plumes in the FT as the cause of enhanced particle concentrations immediately above cloud top.

Relative to RF16, organics accounted for more of the submicrometer nonrefractory aerosol mass concentration, as compared to sulfate in the clear and cloudy columns. The sulfate-to-organic ratio decreased with altitude, and both sulfate and organic mass concentrations were significantly higher above cloud-top altitude, as compared to below cloud. The cloudy side organic mass concentration at wheels-in and FT altitudes was greater than any other concentrations observed in the three flights. Coggon et al. (2014) showed that continental air masses often influence layers above the stratocumulus cloud deck in the study region even though the bulk low-level flow is alongshore; during this flight, biomass-burning plumes were being advected and mixed into the study region from near the Oregon–California border (Maudlin et al. 2015) that are likely linked to the enhanced organic levels observed.

CCN concentrations (0.2% SS) increased above cloud with the most pronounced increase on the cloudy side (from 127 cm^{-3} below cloud to 387 cm^{-3} in the FT). In the cloudy column, D_{act} was higher below cloud (160 nm) and decreased in the wheels-in leg (91 nm) and free troposphere (128 nm), suggestive of more CCN-active aerosol above cloud. On the clear side, D_{act} decreased from 140 nm below cloud to 117 nm in the wheels-in leg and up to 184 nm in the free troposphere. Similar to RF16, the most CCN-active aerosol reside immediately above clouds in the wheels-in leg on both sides of the boundary relative to other level leg altitudes examined.

3) GRADIENTS NEAR CLOUD EDGE

Among the three case flights, observations suggest that during RF19 the cloud edge was the most active and edge dynamics appear to play a contributing role in the

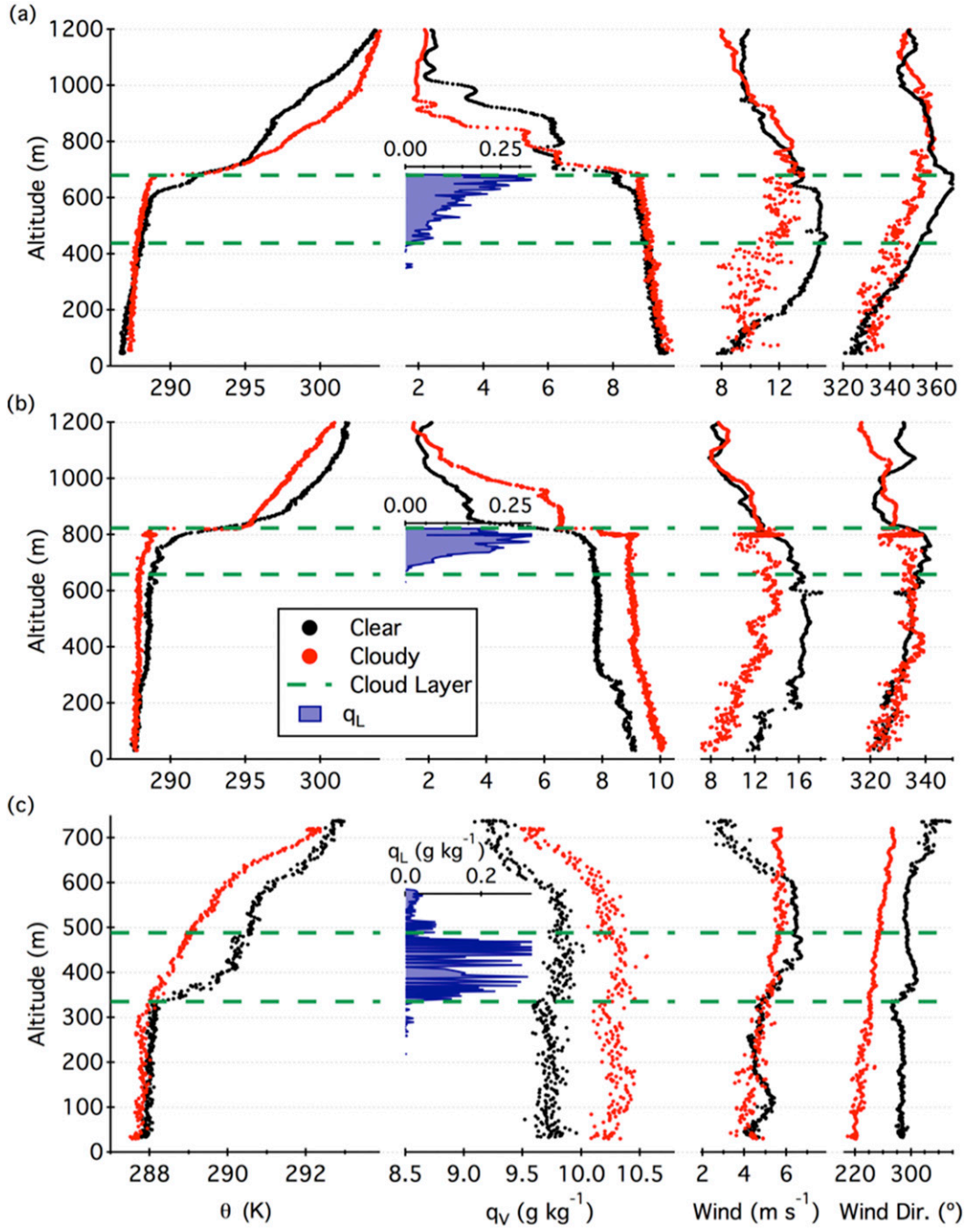

FIG. 6. Sounding profiles in the clear and cloudy columns during the three case flights: (a) RF16, (b) RF19, and (c) RF23.

rapid westward migration of the cloud edge. Thus, a closer analysis is carried out into how winds and thermodynamics varied spatially on the level legs that intercepted the cloud boundary—namely, the above-base and midcloud legs (Fig. 8).

Horizontal winds, resolved into components normal and parallel to the cloud edge, vertical winds, and virtual and equivalent potential temperature anomalies (i.e., value minus the leg-averaged value) are separated into low- and high-frequency components, using a Hanning window filter, with the cutoff approximately representing an eddy-overturning scale (1 km). Both levels indicate that the mean normal wind is from cloudy to clear, which further reinforces that the westward

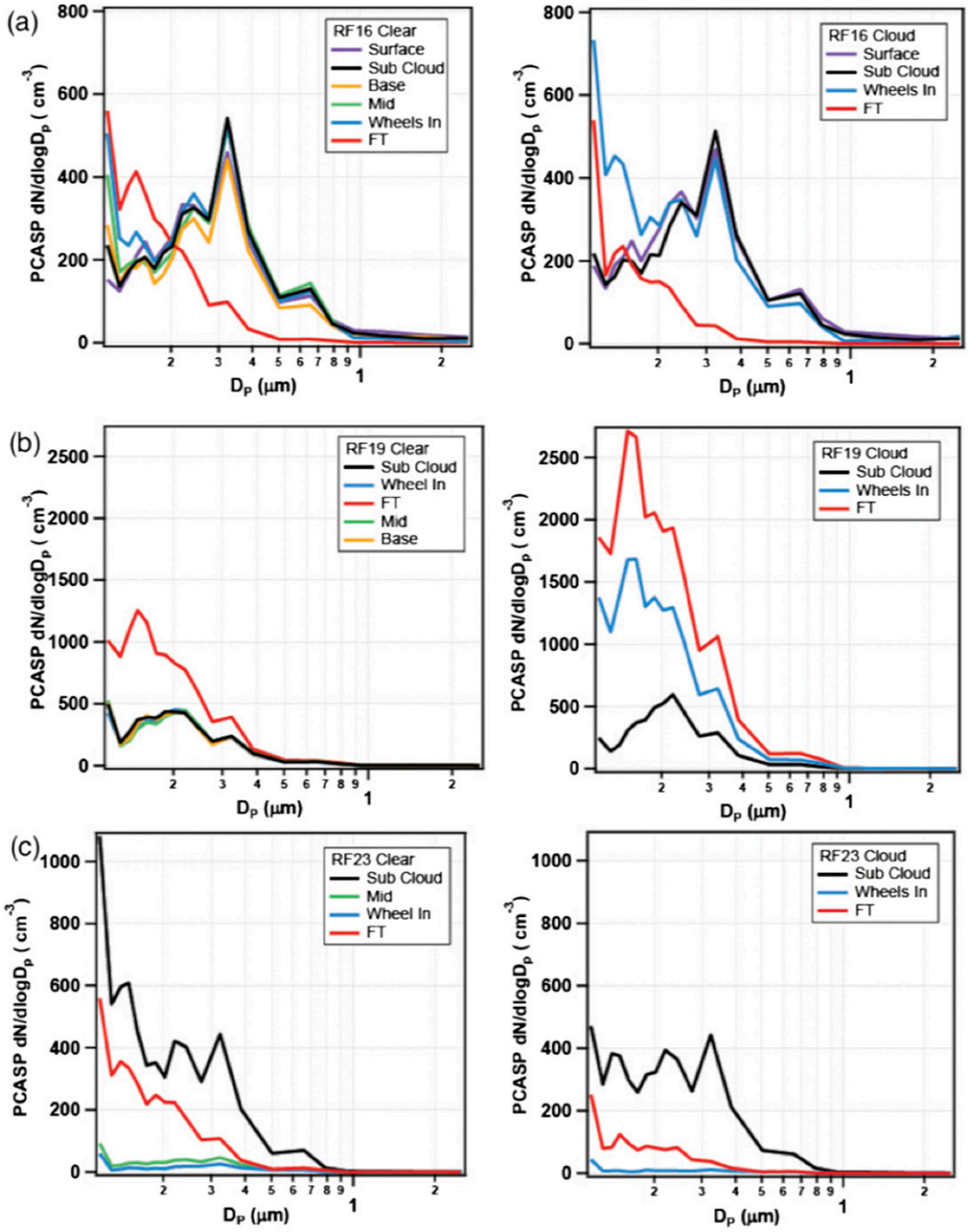

FIG. 7. Vertically resolved PCASP aerosol size distributions during level legs for the three case flights (a) RF16, (b) RF19, and (c) RF23.

clearing expansion cannot be explained by advection of dry air alone. In addition, a pocket of reduced normal flow exists immediately outside of the cloud, which may be associated with the retrograde erosion of the cloud edge. Flow parallel to the cloud edge (from the north-northwest) does not show the same sharp gradient at the edge, although an increase in the wind speed is observed gradually over the transect into the clear air. Negative vertical winds are observed in both transects over a region extending approximately 1 km into cloud, which may be driven by evaporative cooling from lateral entrainment. The gradients in thermodynamic variables are also supportive of this hypothesis that lateral mixing can enhance downdrafts at the cloud edge, particularly

TABLE 4. Instability of mixtures of saturated and unsaturated air in the vicinity of cloud during each flight. Jump conditions are calculated between cloudy air (A), above-cloud air (B), adjacent above-cloud air found in the clearing (C), and air in the clearing horizontally adjacent to cloud (D).

Flight	Jump	θ_e (K)	κ
RF16	A–B	1.3	—
	A–C	0.2	—
	A–D	0.5	—
RF19	A–B	−1.1	0.29
	A–C	−2.8	0.37
	A–D	−3.5	0.69
RF23	A–B	0.5	—
	A–C	0.8	—
	A–D	0.2	—

in the midcloud leg where a local minimum in θ_v exists approximately 1 km inside the cloud edge, close to the downdraft region. Over the same region, a gradual decrease in θ_e is illustrative of lateral mixing across several kilometers. The above-base leg is complicated by the presence of a striking decrease in θ_e deeper into to the cloud, which may also originate from laterally entrained parcels and illustrates the potential three dimensionality of the structure of cloud edge retreat, but further explanation requires additional measurements.

Statistics for the high-frequency fluctuations are summarized through a convolution of 2-km segments across each leg. Covariance of high-pass-filtered normal wind with θ_e and vertical wind with θ_v are used as proxies for lateral mixing and buoyancy production, respectively. Positive buoyancy production is observed throughout the cloud and extends approximately 2 km clear of cloud in both legs. In the midcloud leg, positive θ_e flux acts down the mean θ_e gradient indicating eddy-driven mixing. TKE exhibits similar in-cloud values to the overall leg averages (Table 2) and shows a marked decrease (at least 80%) once clear of clouds. Local maxima are observed in both legs within the first 1–2 km of cloud, further suggestive of edge instability.

f. Case study 3: Research flight 23 (7 August 2013)

1) METEOROLOGICAL AND THERMODYNAMIC SPATIAL PROFILES

As noted previously, RF23 differed from the other two cases in that the clearing was much smaller, the cloudy area was precipitating more heavily, the sampling was later in the afternoon, air above cloud was moister, and the clear–cloudy boundary was closer to land. Analysis of GOES imagery, for 24 h before and after the flight (not shown), suggested that the clearing was short lived and did not become larger than was observed during RF23. Free-tropospheric dewpoint-depression values in RF16 and RF19 (>23°C) greatly exceeded that in RF23 (0.19 ± 0.8°C), indicative of moister air above cloud top in RF23 and the absence of a clear inversion layer above cloud, similar to cases discussed by Christensen and Stephens (2011) and Berner et al. (2015). In-cloud buoyancy production was negative in this case, which contrasted with the other two cases, and it was consistently negative on the clear side except for the wheels-in leg. TKE was again higher in the cloudy column at altitudes below the wheels-in leg, at which point (unlike the other two flights) TKE was higher in the clear column above cloud-relevant altitudes. There was a horizontal wind gradient above the cloud edge, which may be a source of FT turbulence, but it also may be affecting the statistical robustness of the TKE calculation, because the FT survey was limited to a single transect.

The cloud was decoupled from the boundary layer owing likely to stabilization promoted by drizzle evaporation, as has also been observed in pockets of open cells (Terai et al. 2014). This flight had the lowest cloud-base height (340 m), thinnest cloud (150 m), lowest cloud albedo (0.48), and exhibited characteristics of being the cleanest cloud: lowest column-mean drop concentration (N_d = 54 cm^{-3}), highest column-mean drop effective radius (r_e = 14.3 μm), lowest optical depth (7.6), and lowest species mass concentrations in cloud water (Fig. 5).

Unlike RF16 and similar to RF19, significant differences are observed in the clear and cloudy soundings that can explain why clouds were observed on only one side of the boundary: (i) the clear column is slightly warmer in the boundary layer, but in the entire cloud layer it is considerably warmer (>1 K in the upper part of the cloud), and (ii) the clear-side specific humidity was about 0.6 g kg^{-1} lower than the cloudy sounding. There is no evidence of a cloud-top inversion as neither the potential temperature nor water mixing ratio profiles exhibit a jump at cloud top. The inversion base height was about 580 m, but the top of the cloud eroded downward by about 100 m (~490 m). The moisture gradient near 550 m suggests that there may have been a stronger inversion there previously.

The following sequence of events is hypothesized to explain the data. Shortwave absorption by the cloud layer may have caused warming of the upper part of the boundary layer, which could explain why the warming suddenly changes at cloud base. As this air warmed, it decoupled from the surface so it did not mix throughout the boundary layer. In addition, longwave cooling was likely becoming less effective in the thinning cloud layer, further suppressing buoyant mixing from below cloud. A

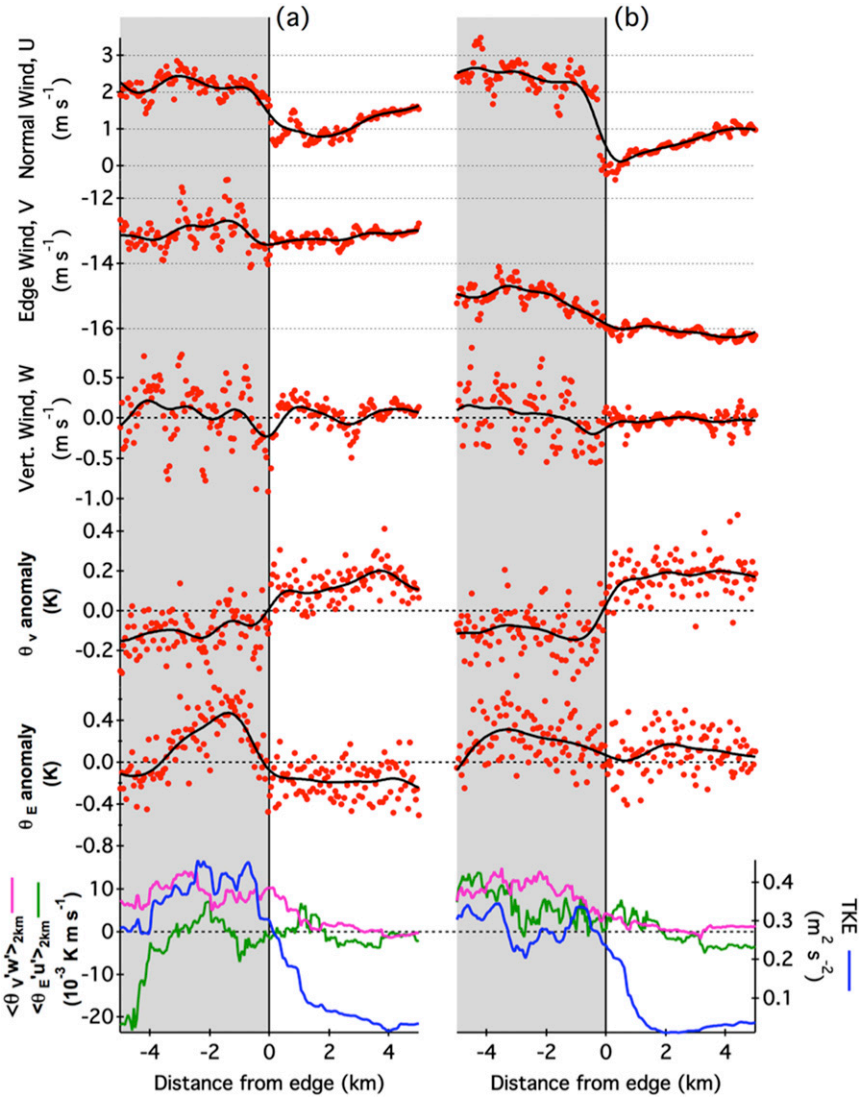

FIG. 8. Horizontal profile of dynamic quantities in the vicinity of cloud edge for (a) above base and (b) midcloud legs. Horizontal winds are resolved into components orthogonal to the cloud edge (normal wind) and parallel to the cloud edge (along-edge wind). Temperature anomalies are calculated with respect to the leg mean. Low-pass-filtered data are overlaid (black). TKE (blue), lateral heat flux (green), and buoyancy flux (magenta) are calculated from 2-km segments.

weak region of cyclonic circulation was located to the northwest of the clearing (Fig. 1) and may have reduced or eliminated the subsidence in the overlying FT air, allowing it to become moistened, and the inversion weakened. At the time of the measurements, substantial entrainment likely still remained because even limited TKE, driven by radiative forcing before the cloud eroded, could cause entrainment through such a weak inversion (1 K). The export of moisture into the FT, the decoupling of the thinning cloud layer from the surface, and potential drying of the boundary layer through drizzle could not be balanced by sufficiently high surface fluxes.

2) AEROSOL SPATIAL PROFILES

Particle number concentrations were much lower above cloud than below and were higher on the clear side as compared to the cloudy side (Table 2). Aside from differences in particle number concentration, the SMPS and PCASP size distributions were similar at all altitudes suggestive of similar particulate sources throughout the two columns, unlike the other

flights. Sulfate was the only nonrefractory species above detection limits and its concentration was much lower above cloud-base heights owing to the decoupling of the cloud layer from surface emissions sources. CCN concentrations dropped from about 55 to 5–17 cm^{-3} above cloud with concomitant enhancements in D_{act} above cloud altitudes due to more hygroscopic aerosol below cloud that was dominated by sulfate.

4. Conclusions

Data from three case flights during the 2013 NiCE campaign are used to discuss vertical and lateral differences in environmental properties across clear–cloudy interfaces in clearings of different sizes off the California coast. The main results are as follows in the order of issues raised at the end of section 1:

(i) Large clearings (≥150 km wide, ≥300 km long) off the California coast occur frequently during summer. One particular clearing observed during NiCE lasted for several days with a diurnal pattern in its width and overall area (expanding during the day; contracting and moving closer to the coast at night). The event exhibited a multiday life cycle, with growth and decay phases, which emerged as a separate mode to the diurnal variability.

(ii) When compared to satellite data, reanalysis data could not accurately capture the spatial pattern of the multiday clearing, motivating greater attention to these features and the underlying factors controlling them.

(iii) Subcloud aerosol, temperature, SST, and wind were similar between clear and cloudy soundings. In one case (RF16), the humidity profile was also very similar; however, in the other two cases (RF19 and RF23) the subcloud column within the clearing was drier. Drying, in these cases, may be explained by a more available source of dry continental air adjacent to the clearing, which is mixed laterally throughout the marine boundary layer. At altitudes comparable with the cloud layer, the clear sounding was warmer than the adjacent cloudy air, explaining the lack of cloud in the clearing; however, in the case of RF16, the warming was confined to approximately the upper 100 m of the cloud layer. The clear air in the closest few hundred meters to the clear–cloudy boundary exhibited an increase in particle effective diameter in RF19 in the boundary layer coincident with negative vertical velocities, suggestive of detrained cloud-processed aerosol. Higher aerosol number concentrations were observed above cloud top in the clear and cloudy columns in the two cases (RF16 and RF19). Although less hygroscopic aerosol is generally observed in the free troposphere in these two flights owing to higher organic fractions, the most CCN-active aerosol were observed in the wheels-in leg owing most likely to a residual layer of cloud-processed aerosol. Significant differences exist above cloud top between the clear and cloudy columns, with aerosol number concentrations differing by up to over a factor of 3.

(iv) The origin, track, and eventual termination of multiday coastal clearings are likely forced by synoptic-scale perturbations in the alignment and strength of the subtropical northeastern Pacific ridge and the resulting interactions with the coastal topography. Low-level trajectories nearly parallel to the coastline during RF16 and RF19 favor increased interaction with continental air through land–sea breeze circulation patterns and can potentially generate horizontal gradients through interactions with coastal headlands. The resulting mesoscale injection of dry air or change to the stability can modulate the extent of the clearing and the rate of expansion or contraction. Analysis of possible buoyancy reversal caused by mixing of cloudy air with adjacent clear air suggests that horizontal entrainment of dry air may be an important contributor to the breakup of the cloud during RF19.

In summary, these results indicate that subtle changes in thermodynamic structure can distinguish a cloud clearing event, even though other environmental variables remain unchanged. Future airborne measurements should specifically target the boundary region to develop a more statistically robust picture of the edge dynamics during both active and quiescent periods. Nocturnal measurements, including vertical profiles and horizontal gradients, during rapidly contracting clearings are also needed.

Acknowledgments. All data used can be obtained from the corresponding author. This work was funded by NASA Grant NNX14AM02G and ONR Grants N00014-11-1-0783, N00014-10-1-0200, and N00014-10-1-0811. JSC acknowledges support from Dreyfus Award EP-11-117. The authors gratefully acknowledge the NOAA Air Resources Laboratory (ARL) for the provision of the HYSPLIT transport and dispersion model and READY website (http://ready.arl.noaa.gov) used in this publication. Some of the analyses and visualizations used in this study were produced with the Giovanni

online data system, developed and maintained by the NASA GES DISC.

REFERENCES

Albrecht, B. A., M. P. Jensen, and W. J. Syrett, 1995: Marine boundary-layer structure and fractional cloudiness. *J. Geophys. Res.*, **100**, 14 209–14 222, doi:10.1029/95JD00827.

Altaratz, O., R. Z. Bar-Or, U. Wollner, and I. Koren, 2013: Relative humidity and its effect on aerosol optical depth in the vicinity of convective clouds. *Environ. Res. Lett.*, **8**, 034025, doi:10.1088/1748-9326/8/3/034025.

Bar-Or, R. Z., I. Koren, O. Altaratz, and E. Fredj, 2012: Radiative properties of humidified aerosols in cloudy environment. *Atmos. Res.*, **118**, 280–294, doi:10.1016/j.atmosres.2012.07.014.

Baumgardner, D., H. Jonsson, W. Dawson, D. O'Connor, and R. Newton, 2001: The cloud, aerosol and precipitation spectrometer: A new instrument for cloud investigations. *Atmos. Res.*, **59–60**, 251–264, doi:10.1016/S0169-8095(01)00119-3.

Berner, A. H., C. S. Bretherton, and R. Wood, 2015: Large-eddy simulation of ship tracks in the collapsed marine boundary layer: A case study from the Monterey area ship track experiment. *Atmos. Chem. Phys.*, **15**, 5851–5871, doi:10.5194/acp-15-5851-2015.

Bony, S., and J.-L. Dufresne, 2005: Marine boundary layer clouds at the heart of tropical cloud feedback uncertainties in climate models. *Geophys. Res. Lett.*, **32**, L20806, doi:10.1029/2005GL023851.

——, and Coauthors, 2006: How well do we understand and evaluate climate change feedback processes? *J. Climate*, **19**, 3445–3482, doi:10.1175/JCLI3819.1.

Bretherton, C. S., and M. C. Wyant, 1997: Moisture transport, lower-tropospheric stability, and decoupling of cloud-topped boundary layers. *J. Atmos. Sci.*, **54**, 148–167, doi:10.1175/1520-0469(1997)054<0148:MTLTSA>2.0.CO;2.

Brewer, M. C., C. F. Mass, and B. E. Potter, 2012: The West Coast thermal trough: Climatology and synoptic evolution. *Mon. Wea. Rev.*, **140**, 3820–3843, doi:10.1175/MWR-D-12-00078.1.

Brooks, I. M., S. Söderberg, and M. Tjernström, 2003: The turbulence structure of the stable atmospheric boundary layer around a coastal headland: Aircraft observations and modelling results. *Bound.-Layer Meteor.*, **107**, 531–559, doi:10.1023/A:1022822306571.

Carman, J. K., D. L. Rossiter, D. Khelif, H. H. Jonsson, I. C. Faloona, and P. Y. Chuang, 2012: Observational constraints on entrainment and the entrainment interface layer in stratocumulus. *Atmos. Chem. Phys.*, **12**, 11 135–11 152, doi:10.5194/acp-12-11135-2012.

Chand, D., and Coauthors, 2012: Aerosol optical depth enhancement in partly cloudy conditions. *J. Geophys. Res.*, **117**, D17207, doi:10.1029/2012JD017894.

Chen, Y. C., M. W. Christensen, L. Xue, A. Sorooshian, G. L. Stephens, R. M. Rasmussen, and J. H. Seinfeld, 2012: Occurrence of lower cloud albedo in ship tracks. *Atmos. Chem. Phys.*, **12**, 8223–8235, doi:10.5194/acp-12-8223-2012.

Christensen, M. W., and G. L. Stephens, 2011: Microphysical and macrophysical responses of marine stratocumulus polluted by underlying ships: Evidence of cloud deepening. *J. Geophys. Res.*, **116**, D03201, doi:10.1029/2010JD014638.

Coggon, M. M., and Coauthors, 2012: Ship impacts on the marine atmosphere: Insights into the contribution of shipping emissions to the properties of marine aerosol and clouds. *Atmos. Chem. Phys.*, **12**, 8439–8458, doi:10.5194/acp-12-8439-2012.

——, and Coauthors, 2014: Observations of continental biogenic impacts on marine aerosol and clouds off the coast of California. *J. Geophys. Res. Atmos.*, **119**, 6724–6748, doi:10.1002/2013JD021228.

Deardorff, J. W., 1980: Cloud top entrainment instability. *J. Atmos. Sci.*, **37**, 131–147, doi:10.1175/1520-0469(1980)037<0131:CTEI>2.0.CO;2.

Draxler, R. R., and G. D. Hess, 1997: Description of the HYSPLIT_4 Modeling System. NOAA Air Resources Laboratory Tech. Memo. ERL ARL-224, 27 pp. [Available online at http://www.arl.noaa.gov/documents/reports/arl-224.pdf.]

Drewnick, F., and Coauthors, 2005: A new time-of-flight Aerosol Mass Spectrometer (TOF-AMS)—Instrument description and first field deployment. *Aerosol Sci. Technol.*, **39**, 637–658, doi:10.1080/02786820500182040.

Duong, H. T., A. Sorooshian, and G. Feingold, 2011: Investigating potential biases in observed and modeled metrics of aerosol-cloud-precipitation interactions. *Atmos. Chem. Phys.*, **11**, 4027–4037, doi:10.5194/acp-11-4027-2011.

Felsch, P., and W. Whitlatch, 1993: Stratus surge prediction along the central California coast. *Wea. Forecasting*, **8**, 204–213, doi:10.1175/1520-0434(1993)008<0204:SSPATC>2.0.CO;2.

Gerber, H., B. G. Arends, and A. S. Ackerman, 1994: New microphysics sensor for aircraft use. *Atmos. Res.*, **31**, 235–252, doi:10.1016/0169-8095(94)90001-9.

——, G. Frick, S. P. Malinowski, H. Jonsson, D. Khelif, and S. K. Krueger, 2013: Entrainment rates and microphysics in POST stratocumulus. *J. Geophys. Res. Atmos.*, **118**, 12 094–12 109, doi:10.1002/jgrd.50878.

Hegg, D. A., and P. V. Hobbs, 1986: Sulfate and nitrate chemistry in cumuliform clouds. *Atmos. Environ.*, **20**, 901–909, doi:10.1016/0004-6981(86)90274-X.

Hersey, S. P., A. Sorooshian, S. M. Murphy, R. C. Flagan, and J. H. Seinfeld, 2009: Aerosol hygroscopicity in the marine atmosphere: A closure study using high-time-resolution, multiple-RH DASH-SP and size-resolved C-ToF-AMS data. *Atmos. Chem. Phys.*, **9**, 2543–2554, doi:10.5194/acp-9-2543-2009.

Klein, S. A., and D. L. Hartmann, 1993: The seasonal cycle of low stratiform clouds. *J. Climate*, **6**, 1587–1606, doi:10.1175/1520-0442(1993)006<1587:TSCOLS>2.0.CO;2.

Kloesel, K. A., 1992: Marine stratocumulus cloud clearing episodes observed during FIRE. *Mon. Wea. Rev.*, **120**, 565–578, doi:10.1175/1520-0493(1992)120<0565:MSCCEO>2.0.CO;2.

Koracin, D., and C. E. Dorman, 2001: Marine atmospheric boundary layer divergence and clouds along California in June 1996. *Mon. Wea. Rev.*, **129**, 2040–2056, doi:10.1175/1520-0493(2001)129<2040:MABLDA>2.0.CO;2.

Kuo, H. C., and W. H. Schubert, 1988: Stability of cloud-topped boundary layers. *Quart. J. Roy. Meteor. Soc.*, **114**, 887–916, doi:10.1002/qj.49711448204.

Lacis, A. A., and J. E. Hansen, 1974: Parameterization for absorption of solar radiation in the earth's atmosphere. *J. Atmos. Sci.*, **31**, 118–133, doi:10.1175/1520-0469(1974)031<0118:APFTAO>2.0.CO;2.

Martins, J. V., D. Tanré, L. Remer, Y. Kaufman, S. Mattoo, and R. Levy, 2002: MODIS Cloud screening for remote sensing of aerosols over oceans using spatial variability. *Geophys. Res. Lett.*, **29**, doi:10.1029/2001GL013252.

Mass, C. F., and M. D. Albright, 1987: Coastal southerlies and alongshore surges of the west coast of North America: Evidence of mesoscale topographically trapped response to

synoptic forcing. *Mon. Wea. Rev.*, **115**, 1707–1738, doi:10.1175/1520-0493(1987)115<1707:CSAASO>2.0.CO;2.

——, and N. A. Bond, 1996: Coastally trapped wind reversals along the United States West Coast during the warm season. Part II: Synoptic evolution. *Mon. Wea. Rev.*, **124**, 446–461, doi:10.1175/1520-0493(1996)124<0446:CTWRAT>2.0.CO;2.

——, M. D. Albright, and D. J. Brees, 1986: The onshore surge of marine air into the Pacific Northwest: A coastal region of complex terrain. *Mon. Wea. Rev.*, **114**, 2602–2627, doi:10.1175/1520-0493(1986)114<2602:TOSOMA>2.0.CO;2.

Maudlin, L. C., Z. Wang, H. H. Jonsson, and A. Sorooshian, 2015: Impact of wildfires on size-resolved aerosol composition at a coastal California site. *Atmos. Environ.*, **119**, 59–68, doi:10.1016/j.atmosenv.2015.08.039.

Mellado, J. P., 2010: The evaporatively driven cloud-top mixing layer. *J. Fluid Mech.*, **660**, 5–36, doi:10.1017/S0022112010002831.

——, B. Stevens, H. Schmidt, and N. Peters, 2009: Buoyancy reversal in cloud-top mixing layers. *Quart. J. Roy. Meteor. Soc.*, **135**, 963–978, doi:10.1002/qj.417.

Nuss, W. A., and Coauthors, 2000: Coastally trapped wind reversals: Progress toward understanding. *Bull. Amer. Meteor. Soc.*, **81**, 719–743, doi:10.1175/1520-0477(2000)081<0719:CTWRPT>2.3.CO;2.

Prabhakar, G., B. Ervens, Z. Wang, L. C. Maudlin, M. M. Coggon, H. H. Jonsson, J. H. Seinfeld, and A. Sorooshian, 2014: Sources of nitrate in stratocumulus cloud water: Airborne measurements during the 2011 E-PEACE and 2013 NiCE studies. *Atmos. Environ.*, **97**, 166–173, doi:10.1016/j.atmosenv.2014.08.019.

Rahn, D. A., and T. R. Parish, 2010: Cessation of the 22–25 June 2006 coastally trapped wind reversal. *J. Appl. Meteor. Climatol.*, **49**, 1412–1428, doi:10.1175/2010JAMC2242.1.

Randall, D. A., 1980: Conditional instability of the first kind upside down. *J. Atmos. Sci.*, **37**, 125–130, doi:10.1175/1520-0469(1980)037<0125:CIOTFK>2.0.CO;2.

——, and M. J. Suarez, 1984: On the dynamics of stratocumulus formation and dissipation. *J. Atmos. Sci.*, **41**, 3052–3057, doi:10.1175/1520-0469(1984)041<3052:OTDOSF>2.0.CO;2.

Remer, L. A., S. Mattoo, R. C. Levy, A. Heidinger, R. B. Pierce, and M. Chin, 2012: Retrieving aerosol in a cloudy environment: Aerosol product availability as a function of spatial resolution. *Atmos. Meas. Tech.*, **5**, 1823–1840, doi:10.5194/amt-5-1823-2012.

Rienecker, M. M., and Coauthors, 2011: MERRA: NASA's Modern-Era Retrospective Analysis for Research and Applications. *J. Climate*, **24**, 3624–3648, doi:10.1175/JCLI-D-11-00015.1.

Roberts, G. C., and A. Nenes, 2005: A continuous-flow streamwise thermal-gradient CCN chamber for atmospheric measurements. *Aerosol Sci. Technol.*, **39**, 206–221, doi:10.1080/027868290913988.

Russell, L. M., and Coauthors, 2013: Eastern Pacific Emitted Aerosol Cloud Experiment. *Bull. Amer. Meteor. Soc.*, **94**, 709–729, doi:10.1175/BAMS-D-12-00015.1.

Sharon, T. M., B. A. Albrecht, H. H. Jonsson, P. Minnis, M. M. Khaiyer, T. M. van Reken, J. Seinfeld, and R. Flagan, 2006: Aerosol and cloud microphysical characteristics of rifts and gradients in maritime stratocumulus clouds. *J. Atmos. Sci.*, **63**, 983–997, doi:10.1175/JAS3667.1.

Shingler, T., and Coauthors, 2012: Characterisation and airborne deployment of a new counterflow virtual impactor inlet. *Atmos. Meas. Tech.*, **5**, 1259–1269, doi:10.5194/amt-5-1259-2012.

Soden, B. J., and G. A. Vecchi, 2011: The vertical distribution of cloud feedback in coupled ocean-atmosphere models. *Geophys. Res. Lett.*, **38**, L12704, doi:10.1029/2011GL047632.

Sorooshian, A., M. L. Lu, F. J. Brechtel, H. Jonsson, G. Feingold, R. C. Flagan, and J. H. Seinfeld, 2007: On the source of organic acid aerosol layers above clouds. *Environ. Sci. Technol.*, **41**, 4647–4654, doi:10.1021/es0630442.

——, Z. Wang, M. M. Coggon, H. H. Jonsson, and B. Ervens, 2013: Observations of sharp oxalate reductions in stratocumulus clouds at variable altitudes: Organic acid and metal measurements during the 2011 E-PEACE campaign. *Environ. Sci. Technol.*, **47**, 7747–7756, doi:10.1021/es4012383.

Stevens, B., G. Vali, K. Comstock, R. Wood, M. C. Van Zanten, P. H. Austin, C. S. Bretherton, and D. H. Lenschow, 2005: Pockets of open cells and drizzle in marine stratocumulus. *Bull. Amer. Meteor. Soc.*, **86**, 51–57, doi:10.1175/BAMS-86-1-51.

Sunuararajan, R., and M. Tjernström, 2000: Observations and simulations of a non-stationary coastal atmospheric boundary layer. *Quart. J. Roy. Meteor. Soc.*, **126**, 445–476, doi:10.1002/qj.49712656305.

Terai, C. R., C. S. Bretherton, R. Wood, and G. Painter, 2014: Aircraft observations of aerosol, cloud, precipitation, and boundary layer properties in pockets of open cells over the southeast Pacific. *Atmos. Chem. Phys.*, **14**, 8071–8088, doi:10.5194/acp-14-8071-2014.

Twohy, C. H., J. A. Coakley, and W. R. Tahnk, 2009: Effect of changes in relative humidity on aerosol scattering near clouds. *J. Geophys. Res.*, **114**, D05205, doi:10.1029/2008JD010991.

Wang, H., and G. Feingold, 2009: Modeling mesoscale cellular structures and drizzle in marine stratocumulus. Part I: Impact of drizzle on the formation and evolution of open cells. *J. Atmos. Sci.*, **66**, 3237–3256, doi:10.1175/2009JAS3022.1.

Wang, Y. G., and B. Geerts, 2010: Humidity variations across the edge of trade wind cumuli: Observations and dynamical implications. *Atmos. Res.*, **97**, 144–156, doi:10.1016/j.atmosres.2010.03.017.

Wang, Z., A. Sorooshian, G. Prabhakar, M. M. Coggon, and H. H. Jonsson, 2014: Impact of emissions from shipping, land, and the ocean on stratocumulus cloud water elemental composition during the 2011 E-PEACE field campaign. *Atmos. Environ.*, **89**, 570–580, doi:10.1016/j.atmosenv.2014.01.020.

Wonaschütz, A., and Coauthors, 2012: Aerosol and gas redistribution by shallow cumulus clouds: An investigation using airborne measurements. *J. Geophys. Res.*, **117**, D17202, doi:10.1029/2012JD018089.

——, and Coauthors, 2013: Hygroscopic properties of smoke-generated organic aerosol particles emitted in the marine atmosphere. *Atmos. Chem. Phys.*, **13**, 9819–9835, doi:10.5194/acp-13-9819-2013.

Wood, R., 2012: Stratocumulus clouds. *Mon. Wea. Rev.*, **140**, 2373–2423, doi:10.1175/MWR-D-11-00121.1.

——, C. S. Bretherton, and D. L. Hartmann, 2002: Diurnal cycle of liquid water path over the subtropical and tropical oceans. *Geophys. Res. Lett.*, **29**, 2092, doi:10.1029/2002GL015371.

Wyant, M. C., M. Khairoutdinov, and C. S. Bretherton, 2006: Climate sensitivity and cloud response of a GCM with a superparameterization. *Geophys. Res. Lett.*, **33**, L06714, doi:10.1029/2005GL025464.

Zhang, Y., B. Stevens, B. Medeiros, and M. Ghil, 2009: Low-cloud fraction, lower-tropospheric stability, and large-scale divergence. *J. Climate*, **22**, 4827–4844, doi:10.1175/2009JCLI2891.1.

Zhu, P. B., and Coauthors, 2005: Intercomparison and interpretation of single-column model simulations of a nocturnal stratocumulus-topped marine boundary layer. *Mon. Wea. Rev.*, **133**, 2741–2758, doi:10.1175/MWR2997.1.